

DETECTION OF DIFFUSE X-RAY EMISSION FROM PLANETARY NEBULAE WITH NEBULAR O VI

N. RUIZ¹, Y.-H. CHU², R.A. GRUENDL², M.A. GUERRERO¹, R. JACOB³, D. SCHÖNBERNER³, & M. STEFFEN³

Draft version August 26, 2018

ABSTRACT

The presence of O VI ions can be indicative of plasma temperatures of a few $\times 10^5$ K that is expected in heat conduction layers between the hot shocked stellar wind gas at several 10^6 K and the cooler (10^4 K) nebular gas of planetary nebulae (PNe). We have used *FUSE* observations of PNe to search for nebular O VI emission or absorption as a diagnostic of conduction layer to ensure the presence of hot interior gas. Three PNe showing nebular O VI, namely IC 418, NGC 2392, and NGC 6826, have been selected for *Chandra* observations and diffuse X-ray emission is indeed detected in each of these PNe. Among the three, NGC 2392 has peculiarly high diffuse X-ray luminosity and plasma temperature compared with those expected from its stellar wind's mechanical luminosity and terminal velocity. The limited effects of heat conduction on the plasma temperature of a hot bubble at the low terminal velocity of the stellar wind of NGC 2392 may partially account for its high plasma temperature, but the high X-ray luminosity needs to be powered by processes other than the observed stellar wind, probably caused by the presence of an unseen binary companion of the CSPN of NGC 2392. We have compiled relevant information on the X-ray, stellar, and nebular properties of PNe with a bubble morphology and found that the expectations of bubble models including heat conduction compare favorably with the present X-ray observations of hot bubbles around H-rich CSPNe, but have notable discrepancies for those around H-poor [WR] CSPNe. We note that PNe with more massive central stars can produce hotter plasma and higher X-ray surface brightness inside central hot bubbles.

Subject headings: planetary nebulae: general – planetary nebulae: individual (IC 418, NGC 2392, NGC 6826) – stars: winds, outflows – X-rays: ISM

1. INTRODUCTION

Planetary nebulae (PNe) consist of the stellar material ejected by low- and intermediate-mass stars near the end of their evolution, before turning into white dwarfs. The physical structure of a PN is largely determined by the photoionization of the slow, dense wind ejected during the asymptotic giant branch (AGB) phase by the intense stellar radiation field and its interaction with the subsequent fast, tenuous wind emanating from the hot stellar core at terminal velocities up to $\sim 4,000$ km s⁻¹ (Cerruti-Sola & Perinotto 1985; Guerrero et al. 2010). In this interacting stellar-wind model (Kwok 1983), the physical structure of a PN is similar to that of a wind-blown bubble and will comprise (1) a central cavity filled with shocked fast wind at temperatures of 10^7 – 10^8 K, (2) a dense shell of swept-up AGB wind at 10^4 K (the bright ring seen in optical images), and (3) an outer envelope of ionized AGB wind material reshaped by the leading shock set up by ionization (cf. Schmidt-Voigt & Köppen 1987; Marten & Schönberner 1991; Mellema 1994; Villaver et al. 2002; Perinotto et al. 2004). At the interface between the shocked fast wind and the swept-up AGB wind, a contact discontinuity forms and heat conduction is expected to occur (Spitzer 1962). The resulting mass evaporation from the dense nebular shell into the hot interior lowers the tempera-

ture and raises the density of the hot gas (Weaver et al. 1977), significantly increasing the X-ray emissivity. Hydrodynamic models of PNe with heat conduction predict diffuse X-ray emission that should be easily detectable with modern X-ray observatories (e.g., Volk & Kwok 1985; Zhekov & Perinotto 1998; Schönberner et al. 2006; Steffen, Schönberner, & Warmuth 2008).

Chandra and *XMM-Newton* observations of diffuse X-ray emission from PNe have been used to investigate the physical properties of the hot interior gas, which shows plasma temperatures of $(1\text{--}3)\times 10^6$ K and X-ray luminosities $L_X=2\times 10^{30}\text{--}3\times 10^{32}$ erg s⁻¹ (e.g., Chu et al. 2004; Guerrero et al. 2005; Montez et al. 2005; Kastner et al. 2008; Ruiz et al. 2011). The X-ray morphology, low plasma temperatures, and moderate L_X are quantitatively consistent with those expected from bubble models with heat conduction (Steffen, Schönberner, & Warmuth 2008).

To make rigorous comparisons between observations and model predictions of hot gas in PN interiors and to achieve statistical significance in the comparisons, the small sample of PNe with known diffuse X-ray emission needs to be enlarged. While it has been observed that PNe possessing detectable diffuse X-ray emission exhibit sharp inner shells of swept-up AGB wind, the reverse may not be true (Kastner et al. 2012). A more reliable diagnostic to ensure the detection of diffuse X-ray emission from PNe is needed. To this end, we have utilized the collisionally ionized O VI expected in interface layers to diagnose the presence of hot gas. Using archival *Far Ultraviolet Spectroscopic Explorer* (*FUSE*; Moos et al. 2000) observations of PNe, we find three cases, IC 418, NGC 2392, and NGC 6826, exhibiting nebular O VI ab-

nieves@iaa.es

¹ Instituto de Astrofísica de Andalucía, IAA-CSIC, c/ Glorieta de la Astronomía s/n, 18008 Granada, Spain

² Department of Astronomy, University of Illinois, 1002 West Green Street, Urbana, IL 61801, USA

³ Leibniz-Institut für Astrophysik Potsdam (AIP), An der Sternwarte 16, 14482 Potsdam, Germany

TABLE 1
SPACE OBSERVATIONS OF IC 418, NGC 2392, AND NGC 6826

<i>FUSE</i> UV Observations						
Object	Program ID	Aperture	Date	Processing Version	t_{exp} [s]	
IC 418	LWRS	P1151111	2001 Dec 2	CalFUSE v3.2.3	4,440	
NGC 2392	LWRS	B0320601	2001 Feb 21	CalFUSE v3.2.3	2,620	
NGC 6826	MDRS	P1930401	2000 Aug 8	CalFUSE v3.2.3	5,800	
<i>Chandra</i> X-ray Observations						
Object	Observation ID	Instrument & Pointing	Date	Processing Version	t_{obs} [ks]	t_{exp} [ks]
IC 418	7440	ACIS-S S3	2006 Dec 12	DS 7.6.9	51.1	50.4
NGC 2392	7421	ACIS-S S3	2007 Nov 13	DS 7.6.11	58.1	57.4
NGC 6826	7439	ACIS-S S3	2007 Jun 11	DS 7.6.10	34.5	34.1
	8559	ACIS-S S3	2007 Jul 24	DS 7.6.10	15.0	14.9
<i>HST</i> Optical Observations						
Object	Program ID	Instrument & Pointing	Date	Filter	t_{exp} [s]	
IC 418	8773	WFPC2-PC	2001 Oct 3	F502N	600	
NGC 2392	8499	WFPC2-WF3	2000 Jan 11	F656N	100	
NGC 6826	6117	WFPC2-PC	1996 Jan 27	F502N	100	

sorption lines. We have subsequently obtained *Chandra* observations of these three PNe, and indeed diffuse X-ray emission is detected in all three cases. In this paper, we describe the *FUSE* observations of PNe in Section 2, report the *Chandra* observations of the three PNe in Section 3, discuss the X-ray results in the framework of models of PNe formation and evolution in Section 4, and summarize the main conclusions in Section 5.

2. O VI DIAGNOSTIC OF HOT GAS

A PN with hot interior gas will possess an interface layer in which the temperature falls from 10^6 K near the hot gas to 10^4 K in the cool nebular shell. Thermal collisions in the interface layer produce highly ionized species, such as C IV, N V, and O VI, whose excitation potentials are 47.8, 77.5, and 113.9 eV, and whose fractional abundances peak at $\sim 1 \times 10^5$, 2×10^5 , and 3×10^5 K, respectively (Shull & van Steenberg 1982). Cloudy simulations (Ferland et al. 1998) show, however, that such ions can also be produced by photoionization in appreciable amounts for luminous central stars of planetary nebulae (CSPNe) hotter than $\sim 35,000$, $85,000$, and $140,000$ K, respectively. Being the hardest to be produced by photoionization, O VI is thus the best choice among the three species for diagnosing interface layers and hot gas in PNe. O VI has a resonance doublet at $\lambda\lambda 1031.9, 1037.6$ Å, a primary spectral feature targeted by *FUSE*.

The O VI doublet from the interface layer can be detected as emission features in *FUSE* spectra if the entrance aperture does not include the CSPN, or as absorption features if the entrance aperture includes the CSPN. *FUSE* observations of NGC 6543 and NGC 7009, two PNe with diffuse X-ray emission, indeed detected nebular O VI emission from the interface layers (Gruendl et al. 2004; Iping et al. 2002).

The *FUSE* archive contains high-dispersion spectra ($\lambda/\Delta\lambda \approx 20,000$, Sahnou et al. 2000) of a large number of CSPNe. These observations provide two pieces of information pertinent to the hot interior gas. First, the stellar O VI lines may show P Cygni profiles indicating the existence of a fast stellar wind that is needed to pro-

duce the hot interior gas in a PN. Second, there may be narrow nebular O VI absorption features superposed on the stellar P Cygni profile, and if the CSPN is cooler than $140,000$ K, the nebular absorption must originate from an interface layer, requiring the existence of hot interior gas. *FUSE* makes simultaneous observations through the $30'' \times 30''$ low (LWRS), $4'' \times 20''$ medium (MDRS), and $1''.25 \times 20''$ high (HIRS) resolution apertures, that are offset from one another. It is possible that some *FUSE* observations of CSPNe had one or two off-source apertures falling within the nebula, allowing us to search for O VI emission from the interface layer.

We have used *FUSE* observations of the nebular shells of a dozen PNe to search for nebular O VI emission, and analyzed *FUSE* observations of $\simeq 60$ CSPNe to search for narrow nebular O VI absorption lines in their spectra. Each observation is typically composed of multiple spectra. The individual exposures were processed using the CalFUSE v3.2.3 (Dixon et al. 2007) to obtain an extracted spectrum. Prior to combining the individual spectra, the relative alignment of each was checked by performing a cross correlation. Typical offsets were less than a few km s^{-1} for the LiF1A module. The spectra were then combined using a weighted average after accounting for the small offsets in wavelength.

Among the PNe with *FUSE* observations, IC 418, NGC 2392, and NGC 6826 display narrow nebular O VI absorption lines superposed on the spectra of their CSPNe (Figure 1, see Table 1 for the details of these observations). We have thus obtained *Chandra* X-ray observations of these three PNe. Note that the *Chandra* observation of NGC 2392 was a follow-up of an earlier *XMM-Newton* observation (Guerrero et al. 2005).

3. CHANDRA OBSERVATIONS

The *Chandra X-ray Observatory* (CXO) observed IC 418, NGC 2392, and NGC 6826 using the array for spectroscopy of the Advanced CCD Imaging Spectrometer (ACIS-S). All three PNe were imaged on the back-illuminated CCD S3 using the VFAINT mode. Details of the observations are given in Table 1. The *Chandra*

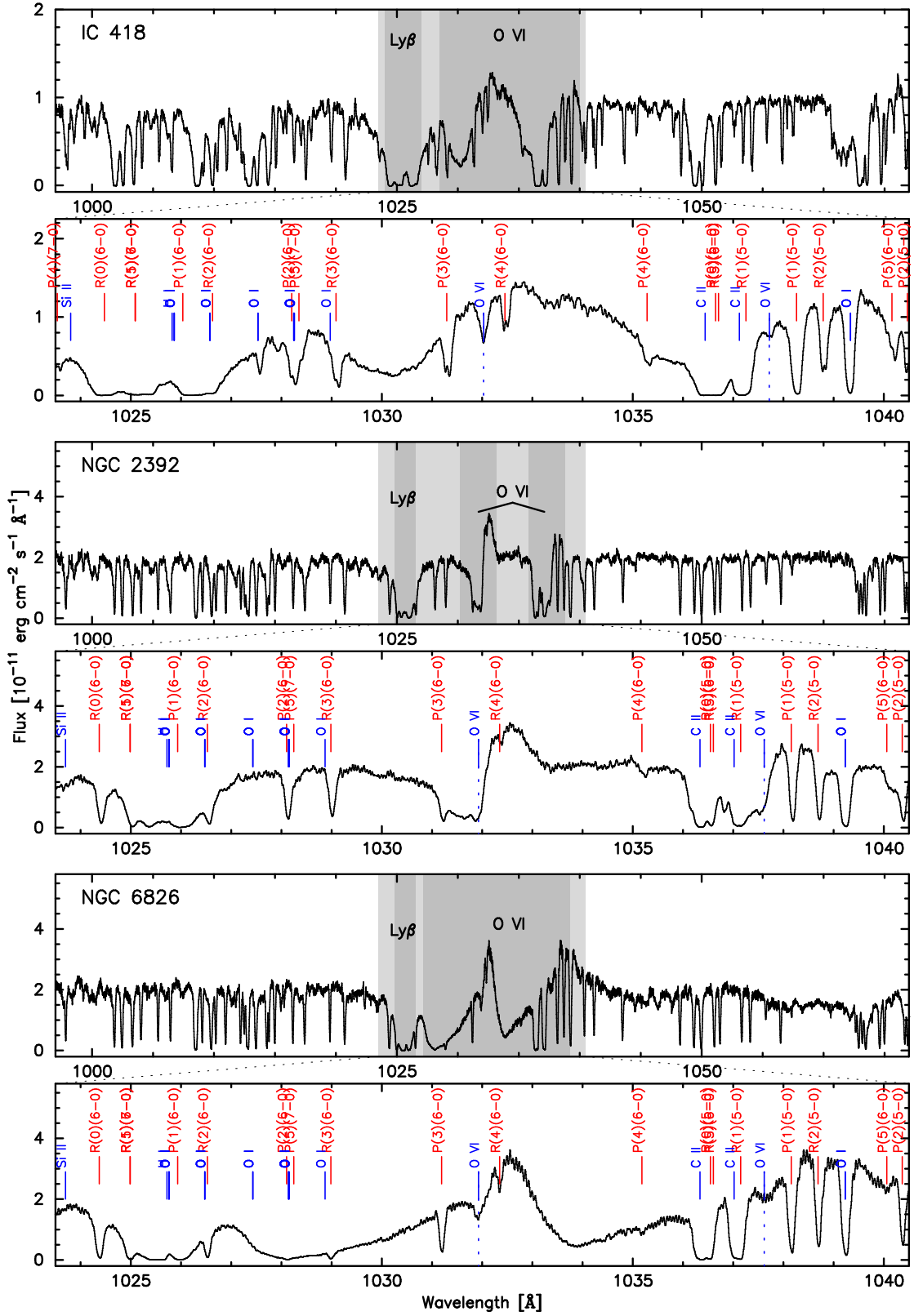


FIG. 1.— *FUSE* spectra showing the region around the O VI lines for the central stars of IC 418 (top panels), NGC 2392 (middle panels), and NGC 6826 (bottom panels). For each object the upper panel shows a wide spectral range with the broad Ly β and O VI P Cygni profiles highlighted (darker grey). The shaded region in the upper panel is expanded to better show narrow absorption features superposed on the broader spectrum. Absorption from the H₂ Lyman and Werner bands are marked in red and ionic transitions are marked with blue. The narrow, nebular O VI components are also marked with vertical dashed lines.

observations of NGC 6826 were split into two segments due to scheduling issues.

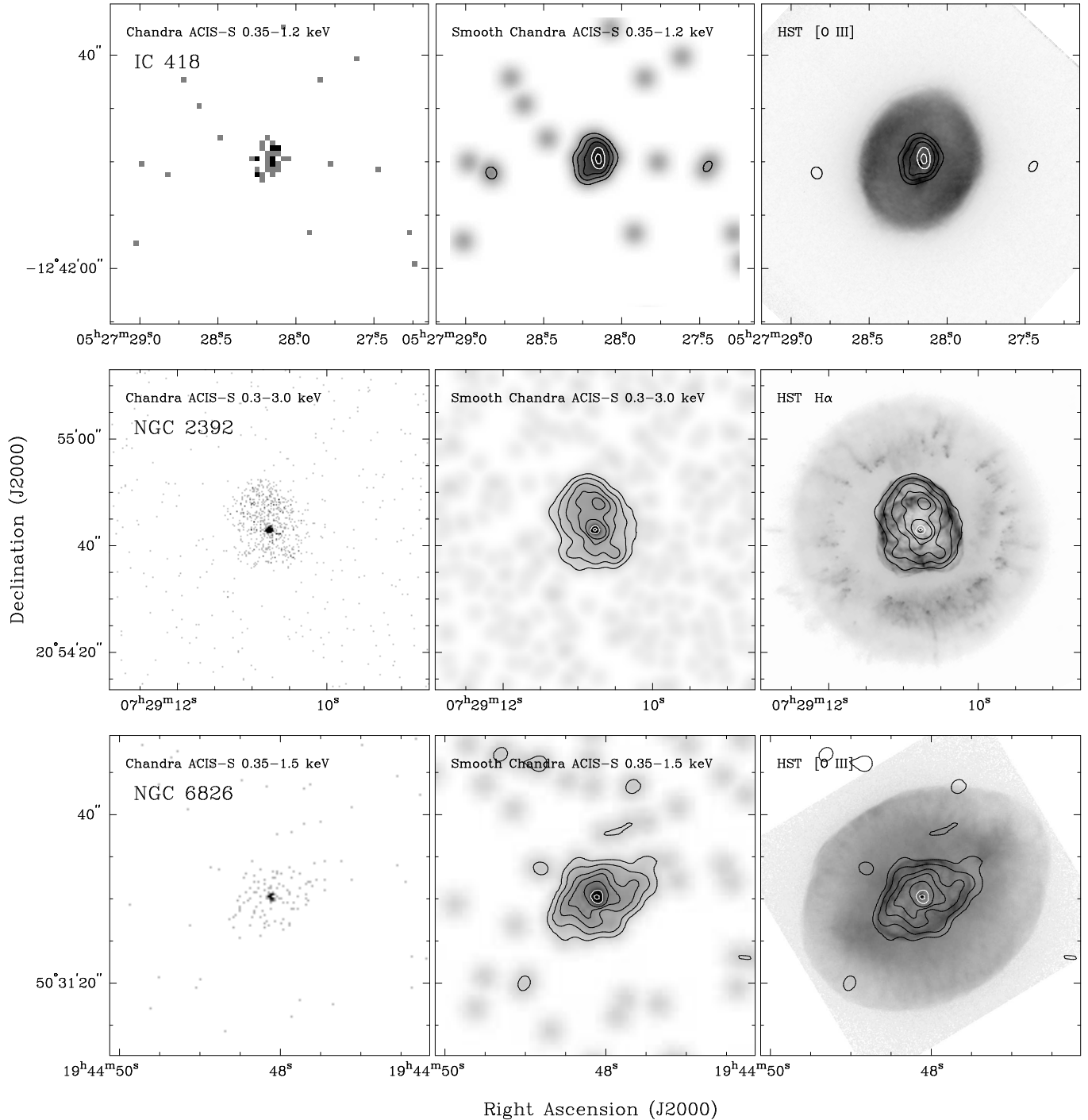


FIG. 2.— *Chandra* ACIS-S raw (left) and smoothed (center) X-ray images and *HST* optical narrow-band images (right) of IC 418 (top row), NGC 2392 (middle row), and NGC 6826 (bottom row). The X-ray contours extracted from the smoothed X-ray images have been overlaid onto the optical images. The black and grey (only for IC 418) contours mark the X-ray levels corresponding to 10%, 25%, 50%, 75%, and 95% of the peak intensity of the diffuse emission. Two additional white contours defining the 25% and 75% of the peak intensity of the central source are shown for NGC 2392 and NGC 6826.

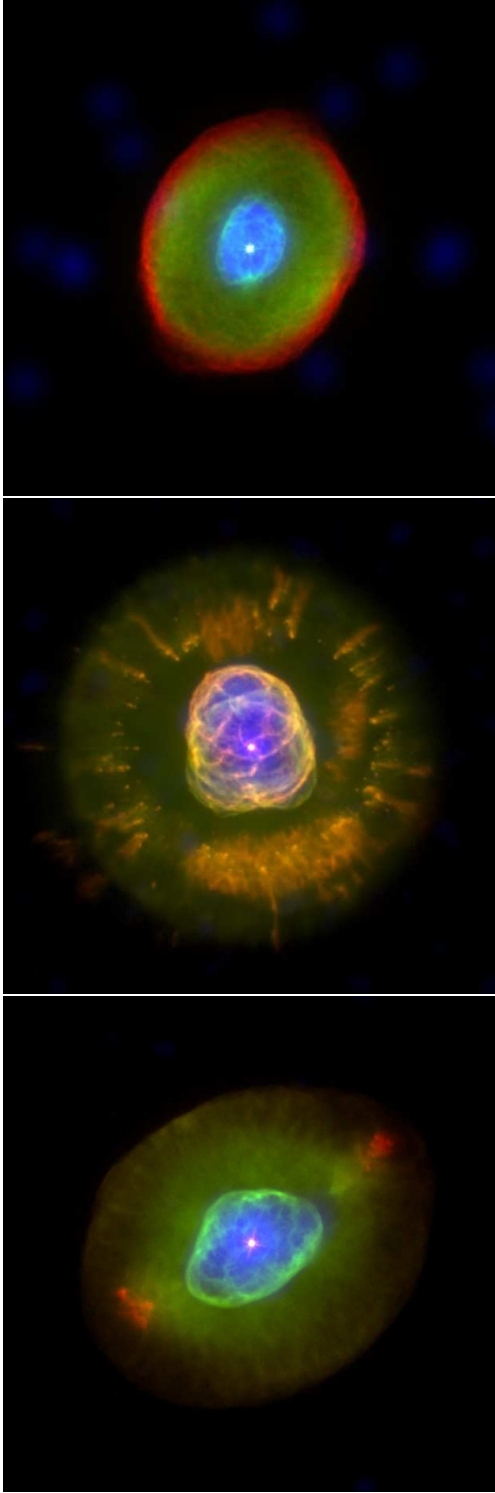


FIG. 3.— *Chandra* and *HST* composite pictures of IC 418 (*upper*), NGC 2392 (*center*), and NGC 6826 (*bottom*). X-ray emission is shown in blue, and optical $H\alpha$ and $[N\ II]$ line emission in green and red, respectively. The field of view (FoV) of the pictures is $\approx 27''$ for IC 418, $\approx 63''$ for NGC 2392, and $\approx 41''$ for NGC 6826.

The background emission level was mostly stable for the observations of the three PNe, with NGC 2392 having a quiescent background level, and IC 418 and NGC 6826 having abnormally high background levels. Besides a short spike of high background that affected the obser-

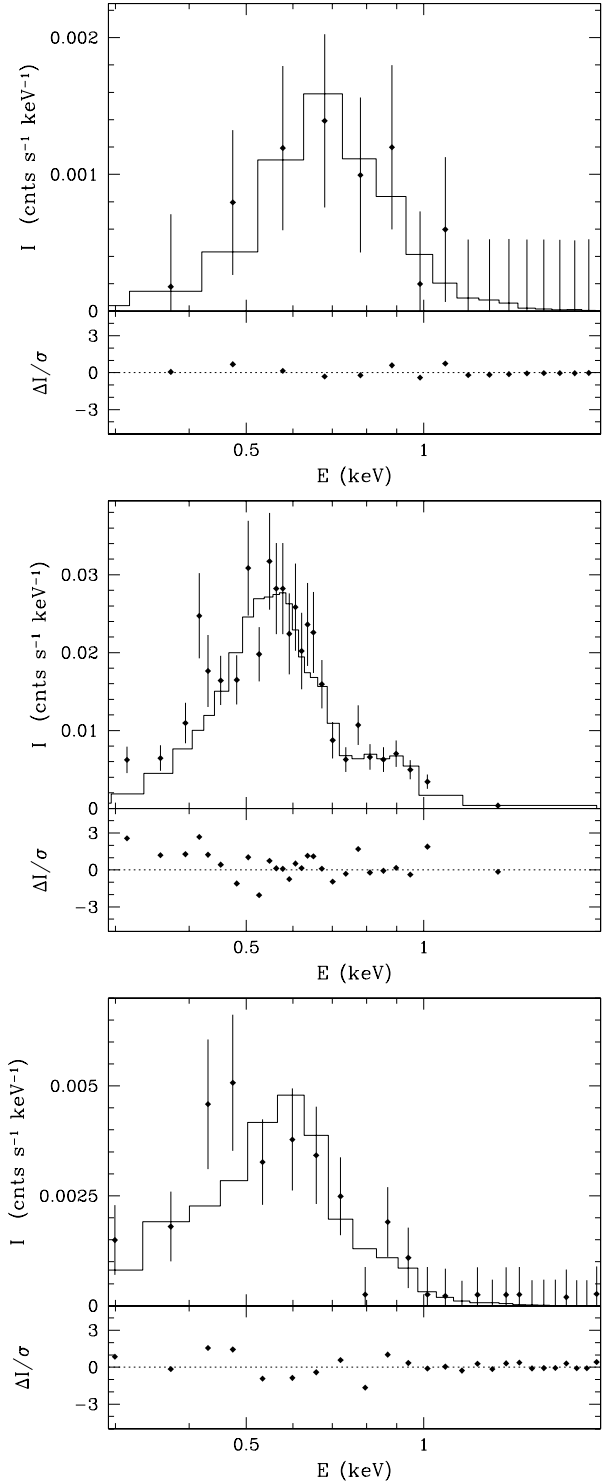


FIG. 4.— *Chandra* ACIS-S S3 background-subtracted spectra of the diffuse X-ray emission of IC 418 (*upper*), NGC 2392 (*center*), and NGC 6826 (*bottom*). The histograms correspond to models that describe well the observed X-ray spectra of IC 418 and NGC 6826, while it is the best-fit model for NGC 2392.

vation of IC 418, no further period has been excised from the original data, and therefore the differences between the observation times t_{obs} and the useful exposure times t_{exp} in Table 1 are mostly associated with the removal of dead-time periods. All subsequent analyses have been

performed using the *Chandra* Interactive Analysis of Observations (CIAO) software package version 4.1.2 and HEASARC XSPEC v12.3.0 routines (Arnaud 1996).

The *Chandra* ACIS-S X-ray images of IC 418, NGC 2392, and NGC 6826 are displayed in Figures 2 and 3. The raw X-ray images in Figure 2 have been extracted using the natural ACIS-S pixel size of $0''.5$. The smoothed images in Figures 2 and 3 have been processed using the CIAO task “*csmooth*” with a circular Gaussian kernel with size up to 4 pixels ($\approx 2''.0$) and a fast-Fourier transform (FFT) convolution method. These images reveal the presence of soft diffuse X-ray emission in the three PNe. A comparison with archival *HST* WFPC2 narrow-band optical images selected to emphasize the innermost shells and small-scale nebular features (Tab. 1) shows that this diffuse X-ray emission is confined within the innermost nebular shell (Figures 2 and 3). We describe below in more detail the spatial and spectral properties of this diffuse emission. The analysis of X-ray point-sources at the CSPNe of NGC 2392 and NGC 6826 will be reported in an upcoming paper (Guerrero et al., in preparation).

3.1. IC 418

The *Chandra* observations of IC 418 detect diffuse emission at an ACIS-S S3 count rate of 0.62 ± 0.12 cnt ks $^{-1}$ in the energy range 0.3-2.0 keV for a total of 32 ± 6 counts. The X-ray emission is confined within the high excitation, innermost $3''.5 \times 5''.0$ shell traced by the emission in the [O III] line (Figs. 2 and 3). Owing to the small angular size of the X-ray-emitting region and small number of counts, the spatial distribution of the X-ray emission cannot be analyzed in detail. Both the raw image and contours on the top panels of Figure 2 suggest that the diffuse X-ray emission is elongated along the major axis of the inner shell. The peak of the X-ray emission is located $\sim 0''.5$ towards the northwest of the location of the central star. The spatial distribution of the diffuse X-ray emission of IC 418 relative to the optical shell and CSPN is reminiscent of that of BD+30 $^{\circ}$ 3639 (Kastner et al. 2000).

The ACIS-S S3 spectrum of IC 418 peaks at $\simeq 0.7$ keV (Figure 4). A spectral fit is obviously not possible, but the observed spectrum can be reasonably well described by a thin plasma emission model with a plasma temperature of 0.26 keV and nebular chemical abundances absorbed by a column density of $N_{\text{H}} \sim 1 \times 10^{21}$ cm $^{-2}$ (Pottasch et al. 2004). In this model, the observed X-ray flux in the 0.3-2.0 keV band is 2.5×10^{-15} erg cm $^{-2}$ s $^{-1}$, and the intrinsic X-ray luminosity is 8.4×10^{29} erg s $^{-1}$ for a distance of 1.2 kpc (Frew 2008). These values are compiled in Table 2, which includes other X-ray properties such as the hot bubble radius and unabsorbed X-ray surface brightness.

3.2. NGC 2392

The *Chandra* observations of NGC 2392 resolve the X-ray emission detected by previous *XMM-Newton* observations (Guerrero et al. 2005) into a point-source at the central star and diffuse emission within the innermost shell of this nebula (Figures 2 and 3). The diffuse emission is well confined within the $15''.2 \times 17''.6$ innermost nebular shell of NGC 2392. Its ACIS-S S3 count rate

in the energy range 0.3-1.5 keV is 9.3 ± 0.4 cnt ks $^{-1}$, and a total of 530 ± 25 counts are detected. The diffuse X-ray emission does not show a limb-brightened morphology, but it is brighter in the central region and towards a northern region inside the central cavity. The spatial distribution of this X-ray emission is roughly consistent with that expected for an ellipsoidal shell filled with hot gas.

The ACIS-S S3 spectrum of the diffuse emission of NGC 2392 peaks at 0.5-0.6 keV and shows a plateau of fainter emission between 0.7 and 1.0 keV. Very little emission is detected above 1.0 keV. The ACIS-S spectrum can be well fit by a thin plasma MEKAL emission model. The analysis of the *XMM-Newton* data (Guerrero et al. 2005) suggested that the X-ray-emitting plasma in NGC 2392 had N/O and Ne/O abundance ratios greater than the respective nebular values of 0.4 and 0.2 (Barker 1991; Henry, Kwitter, & Bates 2000). The more recent nebular abundance study of NGC 2392 by Pottasch et al. (2008) suggests N/O=0.65 and Ne/O=0.30. These nebular abundances, together with the absorption column density $N_{\text{H}}=9 \times 10^{20}$ cm $^{-2}$ converted from the optical extinction, provide a reasonably good fit to the observed X-ray spectrum (reduced $\chi^2=1.12$) for a plasma temperature of $kT=0.18 \pm 0.04$ keV. In this model, the observed flux in the 0.2-1.5 keV band is 3.9×10^{-14} erg cm $^{-2}$ s $^{-1}$, and the intrinsic X-ray luminosity is 1.8×10^{31} erg s $^{-1}$ for a distance of 1.28 kpc (Frew 2008). Other X-ray properties of NGC 2392 are listed in Table 2.

The comparison between the current spectral fit and that performed on the *XMM-Newton* data obtained on 2004 April 2 needs to take into account that *XMM-Newton* did not resolve the point source at the central star from the diffuse emission. The physical conditions implied by the spectral fits to the diffuse emission detected by *Chandra* ($N_{\text{H}}=9 \times 10^{20}$ cm $^{-2}$, $kT=0.18 \pm 0.04$ keV) and by *XMM-Newton* ($N_{\text{H}}=8 \times 10^{20}$ cm $^{-2}$, $kT=0.18_{-0.03}^{+0.01}$ keV) are consistent, but the observed diffuse X-ray flux derived from *Chandra* ($f_{\text{X}}=3.9 \times 10^{-14}$ erg cm $^{-2}$ s $^{-1}$) is $\sim 35\%$ lower than that from the *XMM-Newton* ($f_{\text{X}}=6.0 \times 10^{-14}$ erg cm $^{-2}$ s $^{-1}$). Part of this difference is caused by the contribution of the central point source, of which the observed flux is 1.4×10^{-14} erg cm $^{-2}$ s $^{-1}$ (Guerrero et al., in preparation). The remaining $\simeq 12\%$ difference is only slightly larger than the calibration uncertainties between *Chandra* ACIS and *XMM-Newton* EPIC⁴.

3.3. NGC 6826

The *Chandra* observations of NGC 6826 detect a point-source at its central star (Guerrero et al., in preparation) and diffuse emission that, as is the case with IC 418 and NGC 2392, is confined within the $\sim 12''.4 \times 7''.4$ innermost shell of the nebula (Figs. 2 and 3). The diffuse emission is detected at an ACIS-S S3 count rate of 1.97 ± 0.21 cnt ks $^{-1}$ in the energy range 0.3-2.0 keV for a total of 96 ± 10 counts. The spatial distribution of the diffuse X-ray emission shown by the contours on the bottom panels

⁴ As described by the *XMM-Newton* Calibration Team in http://xmm.esac.esa.int/external/xmm_calibration, these differences can amount to 10%, especially in the soft energy range below 1 keV.

TABLE 2
X-RAY DETECTIONS OF DIFFUSE EMISSION FROM PNE WITH BUBBLE MORPHOLOGY

Object	Telescope & Instrument	d^a [kpc]	Hot Bubble Radius [pc]	Count Rate [cnt ks ⁻¹]	f_X [erg cm ⁻² s ⁻¹]	S_X^b [erg cm ⁻² s ⁻¹ arcsec ⁻²]	L_X^b [erg s ⁻¹]	kT_X [keV]	Ref.
BD+30°3639	<i>CXO</i> ACIS-S	1.30	0.013	244±4	5.7×10^{-13}	2.2×10^{-14}	2.7×10^{32}	0.233±0.007	1
IC 418	<i>CXO</i> ACIS-S	1.20	0.012	0.62±0.12	2.5×10^{-15}	8.4×10^{-17}	8.4×10^{29}	0.26	2
NGC 40	<i>CXO</i> ACIS-S	1.02	0.10	2.8±0.9	1.3×10^{-14}	8.3×10^{-17}	2.1×10^{31}	0.09	3,4 ^c
NGC 2392	<i>CXO</i> ACIS-S	1.28	0.050	9.3±0.4	3.9×10^{-14}	1.0×10^{-16}	1.8×10^{31}	0.18±0.04	2
NGC 3242	<i>XMM</i> EPIC	1.0	0.041	31.3±1.6	4.2×10^{-14}	5.8×10^{-17}	7.3×10^{30}	0.202±0.011	5
NGC 5315	<i>CXO</i> ACIS-S	2.62	0.017	12.4±0.7	1.0×10^{-13}	1.5×10^{-14}	2.9×10^{32}	0.224±0.022	4
NGC 6543	<i>CXO</i> ACIS-S	1.50	0.037	42.4±0.9	9.5×10^{-14}	5.7×10^{-16}	6.5×10^{31}	0.145±0.010	6
NGC 6826	<i>CXO</i> ACIS-S	1.30	0.028	1.97±0.21	9.0×10^{-15}	3.4×10^{-17}	2.0×10^{30}	0.20	2
NGC 7009	<i>XMM</i> EPIC	1.45	0.051	61.5±1.7	7.2×10^{-14}	1.9×10^{-16}	4.4×10^{31}	0.152±0.015	7
NGC 7027	<i>CXO</i> ACIS-S	0.89	0.012	14.0±0.9	3.1×10^{-14}	5.2×10^{-14}	1.3×10^{32}	0.26	8

REFERENCES. — (1) Kastner et al. (2000), (2) this work, (3) Montez et al. (2005), (4) Kastner et al. (2008), (5) Ruiz et al. (2011), (6) Chu et al. (2001), (7) Guerrero et al. (2005), (8) Kastner et al. (2001).

^a Distances adopted from Mellema (2004) and Frew (2008).

^b Unabsorbed X-ray surface brightness and luminosity in the energy range 0.3-2.0 keV.

^c Montez et al. (2005) mistakenly reported the absorbed X-ray luminosity of NGC 40 whose value was later corrected by Kastner et al. (2008).

of Figure 2 hint at a patchy distribution which seems to be better described by a centrally filled shell than by the limb-brightened morphology that would produce a thin shell.

The ACIS-S S3 spectrum of NGC 6826 is soft, with a plateau of emission between 0.35 and 0.7 keV over which a subtle peak at ~ 0.45 keV can be seen. A weaker emission peak is detected at ~ 0.9 keV, and no noticeable emission is detected above 1.0 keV. The spectral shape is suggestive of emission from an optically thin plasma, but, as with IC 418, no reliable spectral fit is possible due to the small number of counts. Assuming the chemical abundances and absorbing column density of $N_H \sim 1 \times 10^{20}$ cm⁻² derived for NGC 6826 (Surendiranath & Pottasch 2008), the spectrum of its diffuse X-rays can be reasonably well described by a plasma emission model for a plasma temperature of $kT = 0.2$ keV and the observed X-ray flux is 9.0×10^{-15} erg cm⁻² s⁻¹ in the 0.3-2.0 keV energy band. The intrinsic X-ray luminosity for this model and energy band is 2.0×10^{30} erg s⁻¹ for a distance of 1.3 kpc (Frew 2008). Further X-ray properties of NGC 6826 are listed in Table 2.

4. DISCUSSION

The background-subtracted spectra of IC 418, NGC 2392 and NGC 6826 have been described using optically-thin thermal plasma models with nebular abundances and their basic parameters (temperature and X-ray flux and luminosity in the energy band 0.3-2.0 keV) determined in previous sections. The detection of diffuse X-ray emission from these three PNe, together with NGC 6543 and NGC 7009 (Gruendl et al. 2004; Iping et al. 2002), testifies that nebular O VI emission and/or absorption is an excellent diagnostic for the presence of hot bubbles in PNe with sharp shell morphology.

Similarly, the detection of diffuse X-ray emission in a PN can be used to forecast the presence of narrow O VI absorptions in the spectrum of its CSPN. Among the PNe with diffuse X-ray emission (this paper; Kastner et al. 2012), there are another four with

available *FUSE* observations of their central stars in the spectral range of the O VI lines, namely BD+30°3639, NGC 40, NGC 2371-2, and NGC 7662 (Guerrero & De Marco 2013). A careful scrutiny of these spectra reveals narrow O VI absorptions of the $\lambda 1031.9$ Å line in NGC 40, NGC 2371-2, and possibly in NGC 7662, as well as a possible absorption of the $\lambda 1037.6$ Å line in NGC 2371-2. As for BD+30°3639, the search for narrow O VI absorptions in its *FUSE* spectrum is inconclusive because the large number of atomic and H₂ absorption lines that dominate its stellar continuum at this wavelength range. To sum up, 8 out of the 9 PNe with diffuse X-ray emission also show O VI narrow absorptions in the stellar continuum of their CSPNe.

The firm correlation between diffuse X-ray emission and O VI narrow absorptions in the stellar continuum of PNe with sharp shell morphology provides strong evidence for a conduction layer between the hot interior and the cool nebular shell of PNe. The physical structure (how the density and temperature vary with radial distance) of this conduction layer and the amount of highly ionized species present at this interface (O⁺⁵, N⁺⁴) depend on the efficiency of thermal conduction, although the O VI luminosity seems rather insensitive to those effects (Steffen, Schönberner, & Warmuth 2008). We expect our awarded *HST* STIS observations of the N V and C IV line emission from the interfaces in NGC 6543 (PI: M.A. Guerrero) and in the Wolf-Rayet wind-blown bubble S 308 (PI: Y.-H. Chu) would help us obtain more information on the physical structure of conduction layers.

4.1. Hot Bubbles of Planetary Nebulae

Chandra and *XMM-Newton* have yielded a number of detections of diffuse X-ray emission confined within the innermost closed shells of PNe, the so-called hot bubbles. Sources with available X-ray luminosities and temperatures in the literature⁵ are summarized in Table 2 where we have excluded the bipolar PNe Mz 3 and NGC 7026

⁵ Recently, Kastner et al. (2012) has reported the detection of diffuse X-ray emission in the elliptical PNe NGC 2371-2 and NGC 7662, but no estimates of their X-ray temperatures and lu-

TABLE 3
PROPERTIES OF THE STELLAR WIND AND DIFFUSE X-RAY EMISSION OF PNE

Object	Spectral Type	T_{eff} [kK]	v_{∞} [km s $^{-1}$]	$\log L/L_{\odot}^{\text{a}}$	\dot{M}^{a} [M_{\odot} yr $^{-1}$]	$\log(L_{\text{X}}/L_{\star})^{\text{b}}$	$\log(L_{\text{X}}/L_{\text{wind}})^{\text{b}}$	$T_{\text{shock}}^{\text{c}}$ [10^6 K]	$T_{\text{X}}/T_{\text{shock}}$	Ref.
BD+30 $^{\circ}$ 3639	[WC9]	47	700	3.77	1.8×10^{-6}	-4.93	-3.01	14.8	0.2	1
IC 418	Of(H)	39	700	3.72	3.3×10^{-8}	-7.39	-3.78	7.4	0.4	2
NGC 40	[WC8]	71	1000	3.42	1.1×10^{-6}	-5.69	-4.22	30.2	0.035	1
NGC 2392	O6f	45	300	3.82	8.4×10^{-9}	-6.16	-1.12	1.4	1.5	3
NGC 3242	O(H)	75	2400	3.42	3.4×10^{-9}	-6.15	-2.93	87.0	0.03	2
NGC 5315	[WO4]	76	2400	3.74	1.6×10^{-6}	-4.87	-4.00	174.0	0.015	1
NGC 6543	wels	60	1450	3.54	3.3×10^{-8}	-5.32	-2.53	31.8	0.05	2,3
NGC 6826	O3f(H)	44	1200	3.81	4.7×10^{-8}	-7.10	-4.03	22.0	0.1	2
NGC 7009	O(H)	87	2770	3.56	1.2×10^{-9}	-5.51	-1.82	115.9	0.015	4,5,6
NGC 7027	...	198	...	3.89	...	-5.37	7

REFERENCES. — (1) Marcolino et al. (2007), (2) Pauldrach et al. (2004), (3) Herald & Bianchi (2011), (4) Méndez et al. (1988), (5) Cerruti-Sola & Perinotto (1989), (6) Iping et al. (2002), (7) Latter et al. (2000).

^a Stellar luminosities and mass-loss rates adopted from the references in the last column and scaled with the distances given in Table 2.

^b X-ray luminosity in the 0.3-2.0 keV energy band.

^c The shock temperature of the [WR] stars BD+30 $^{\circ}$ 3639, NGC 40, and NGC 5315 is at given wind velocity about twice that of normal CSPNe, according to the larger mean molecular weight of their stellar winds.

(Guerrero, Chu, & Miranda 2004; Gruendl et al. 2006; Clark et al. 2012). Table 2 compiles the X-ray properties of the PNe with bubble morphology, including their observed X-ray flux (f_{X}) and intrinsic surface brightness (S_{X}) and luminosity in the energy band 0.3-2.0 keV, scaled to the distance determined by Frew (2008), as well as the X-ray temperature and hot bubble radius⁶.

It is interesting to compare the physical properties of these CSPNe and their winds with the physical parameters of hot gas inferred from the diffuse X-ray emission. The properties of stellar winds of these PNe have been compiled in Table 3 that includes the stellar spectral type (column 2), effective temperature (column 3), wind terminal velocity (column 4), stellar luminosity (column 5), and mass-loss rate (column 6) as provided by the references listed in the last column of the table. An inspection of the spectral type of the CSPNe reveals that this sample consists of three H-poor [WR] CSPNe (BD+30 $^{\circ}$ 3639, NGC 40, and NGC 5315), and six H-rich CSPNe (IC 418, NGC 2392, NGC 3242, NGC 6543, NGC 6826, NGC 7009, and NGC 7027). The wind terminal velocities, stellar luminosities, and mass-loss rates have been derived from model atmosphere analyses of UV and optical stellar lines, except for NGC 7027 (Latter et al. 2000). We note that the stellar luminosities and mass-loss rates provided here have been scaled with respect to those given in the original references by the distance given in the third column of Table 2.

The X-ray luminosities and temperatures of these nebulae are then compared to their stellar (L_{\star}) and wind mechanical ($L_{\text{wind}} \equiv \frac{1}{2} \dot{M} v_{\infty}^2$) luminosities in columns 7 and 8 of Table 3. Finally, the post-shock temperature of the stellar wind (T_{shock}), estimated assuming an adia-

batic shock as

$$T_{\text{shock}} = \frac{3}{16} \frac{\mu}{k} v_{\infty}^2 \equiv 2.3 \times 10^7 \mu \left(\frac{v_{\infty}}{1000 \text{ km s}^{-1}} \right)^2 \text{ [K]}, \quad (1)$$

where μ is the mean molecular weight⁷, is listed in column 9 and compared with the plasma temperature derived from X-ray spectra in column 10.

These observationally determined properties of hot plasma in PNe are compared in Figure 5 to theoretical predictions based on 1D hydrodynamical simulations performed with the code NEBEL (Perinotto et al. 2004; Steffen, Schönberner, & Warmuth 2008; Steffen et al. 2012). These simulations take into account the energy transfer due to heat conduction and the evolution of stellar mass-loss rate and terminal wind velocity that determine the mechanical energy input into the hot bubble. The plots presented in Figure 5 are thus an increment and refinement of the plots in Steffen, Schönberner, & Warmuth (2008) for a larger sample of PNe with consistently revised stellar properties and diffuse X-ray parameters.

Before starting a discussion on the location of the PNe in our sample on these plots, we would like to note that the models presented in Figure 5 have been developed exclusively for PNe with H-rich central stars. Therefore, the PNe with [WR] central stars BD+30 $^{\circ}$ 3639, NGC 40, and NGC 5315 (marked in these plots by “pink” symbols) are not expected to follow these tracks. Indeed, the data points of these sources appear notably far from these theoretical tracks, e.g., BD+30 $^{\circ}$ 3639 and NGC 5315, with young [WR] CSPNe, exhibit the highest values of L_{X} (Fig. 5-a) and largest L_{X}/L_{\star} ratios (Fig. 5-b, d, and e). Interestingly, the X-ray temperatures predicted by the models for H-rich stellar winds do not differ critically from the temperature of the hot plasma derived for PNe with [WR] CSPNe (Fig. 5-f), despite that they have more massive stellar winds with higher mechanical

minisities are available. Similarly, diffuse X-ray emission has been detected within the innermost shell of IC 4593 (Guerrero et al., in preparation).

⁶ We note here that the values of the hot bubble radii of the PNe in Table 2 that were analyzed by Kastner et al. (2008) clearly differ with their values because they used diameters but quoted them as radii.

⁷ The mean molecular weight for fully ionized H-rich stellar winds can be approximated as ≈ 0.6 , whereas for fully ionized H-poor stellar winds is ≈ 1.2 .

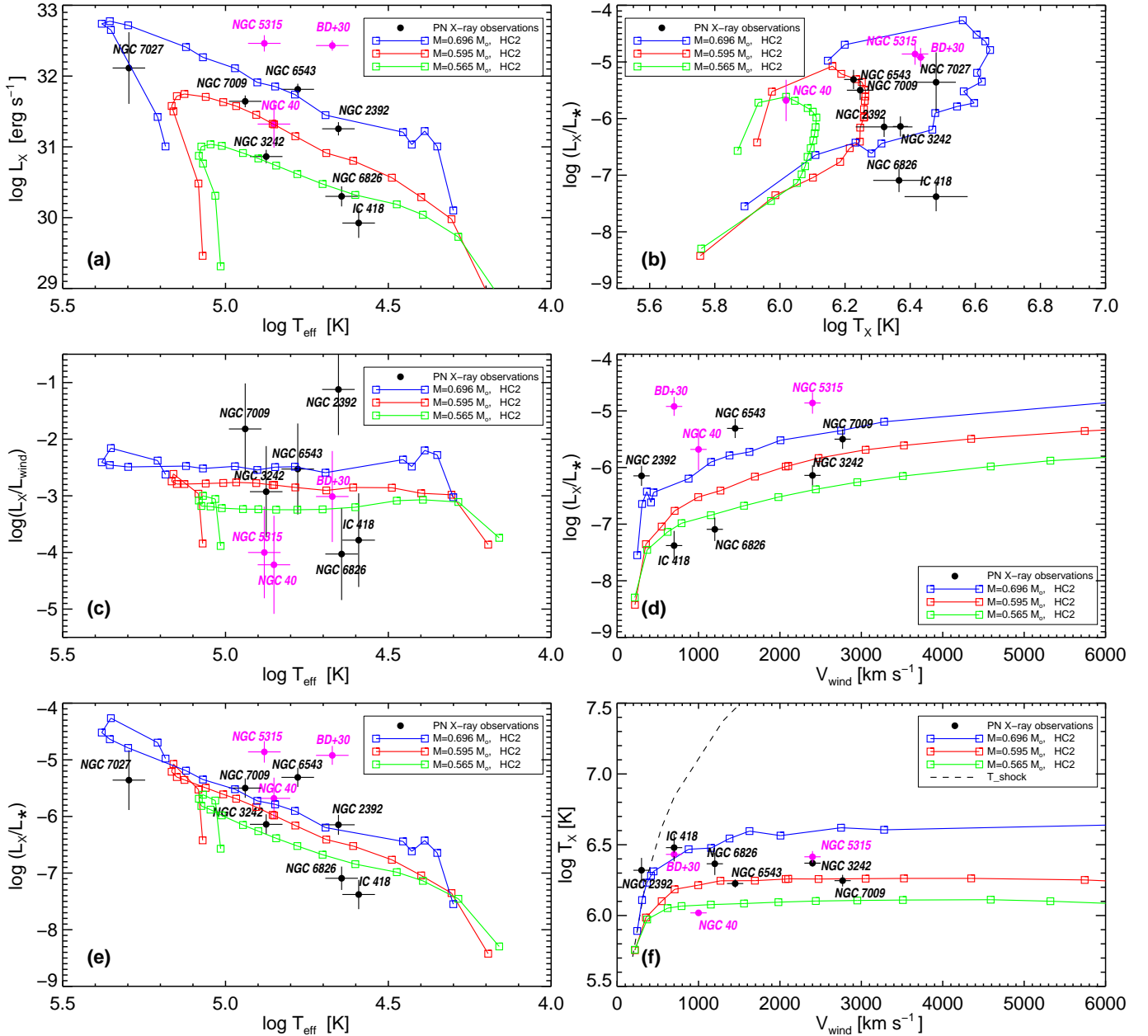


FIG. 5.— X-ray luminosity (L_X) of the hot bubble of PNe for the energy range 0.3–2.0 keV (6.2–41 Å) and X-ray temperature (T_X) as functions of T_{eff} , the stellar effective temperature (panels a, c, and e), X-ray temperature (panel e), and V_{wind} , the wind terminal velocity (panels d and f). In panels b, c, d, and e, L_X has been scaled with the stellar luminosity (L_*) and wind mechanical luminosity (L_{wind}) to remove the dependence on distance. The tracks correspond to the theoretical models HC2 with heat conduction for CSPNe with masses $0.565 M_{\odot}$ (green), $0.595 M_{\odot}$ (red), and $0.696 M_{\odot}$ (blue) according to the prescriptions of the second method used by Steffen, Schönberner, & Warmuth (2008), i.e., the heat flux does not exceed the saturation limit. The dashed line in panel f represents the post-shock temperature of an adiabatic shock for the case of H-rich stars, i.e., T_{shock} described by Eq. 1 for $\mu=0.6$. Black dots correspond to objects with a H-rich CSPN, whereas pink dots refer to sources with a [WR]-type CSPN. The error-bars in the data points correspond to the $1\text{-}\sigma$ uncertainty in our determination of L_X and T_X (the uncertainty in distance is not included in the error-bar of L_X). Typical uncertainties of 0.15 dex for L_* and 0.8 dex for L_{wind} have been convolved with the error-bars of L_X for the L_X/L_* and L_X/L_{wind} ratios. Similarly, typical uncertainties of 0.05 dex in T_{eff} and 100 km s^{-1} in V_{wind} are presented.

luminosities than their H-rich counterparts. Theoretical work is underway to investigate the X-ray properties of hot bubbles around [WR] CSPNe (Steffen et al. 2012).

Overall, there is a good agreement between the global properties of the hot gas in PNe with H-rich stars (“black” symbols in Figure 5) and the model predictions, i.e., most of the data points are bracketed within the tracks predicted by the models. The most notable

differences appear in the comparison between models and observations when the stellar wind mechanical luminosity, L_{wind} , is considered (Fig. 5-c). The dispersion of the data points in this figure can stem from the large uncertainties in the mass-loss estimates, but also from the comparison of the present-time mass loss with X-ray properties that depend on the mass-loss rate integrated over time. The difficulties for such com-

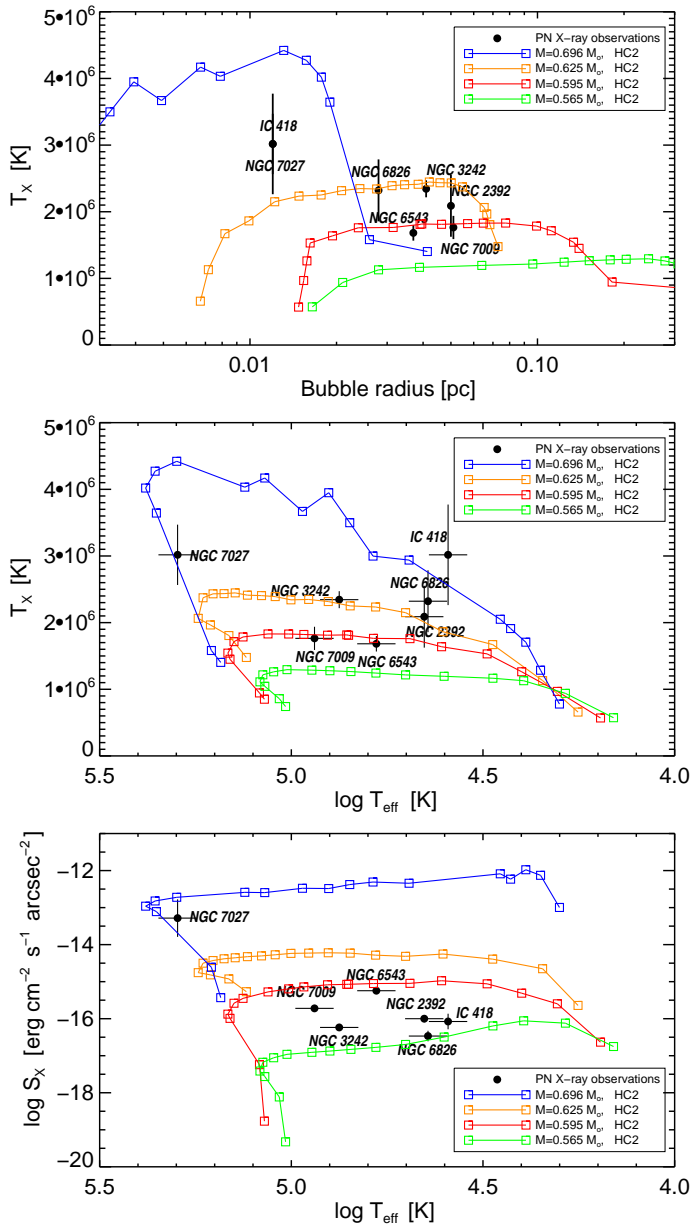


FIG. 6.— Comparisons of the X-ray plasma temperature with hot bubble radius of PNe (*top*) and CSPN effective temperature (*middle*), and X-ray surface brightness with CSPN effective temperature (*bottom*). The theoretical tracks of the variations of T_X and S_X imply that the observations comply with the expectations of the theoretical models HC2 including heat conduction for central stars with masses $0.565 M_\odot$ (green), $0.595 M_\odot$ (red), $0.625 M_\odot$ (orange), and $0.696 M_\odot$ (blue) adopted from Steffen, Schönberner, & Warmuth (2008). Error-bars as in Figure 5.

parison are well illustrated by NGC 7009, whose low mass-loss rate, as provided by Cerruti-Sola & Perinotto (1989), is increased by other authors by factors of ~ 1.8 (Tinkler & Lamers 2002), ~ 3.6 (Bombeck et al. 1986), and ~ 10.7 (Cerruti-Sola & Perinotto 1985). On the other hand, the increase of X-ray luminosity with time, as revealed by the evolution dependent stellar parameters T_{eff} and v_∞ shown in panels a, d, and e of Figure 5, is consistent with the model predictions. Similarly, the little variation of T_X with the evolution predicted by the models is supported by the data points shown in panels

b and f of Figure 5.

As for the PNe with new data presented in this paper, we note that IC 418 and NGC 6826 seem to have low values of L_X and L_X/L_\star , and very notably small L_X/L_{wind} (Fig. 5-c). We should emphasize that the X-ray luminosities of these two PNe have not been derived from spectral fits, but from a rough estimate of their X-ray temperatures and count rates due to the small number of detected counts (~ 32 cnts and ~ 96 cnts, respectively). The uncertainty in the X-ray temperature of these sources can amount up to 15–25%, whereas the count rate uncertainty is $\sim 20\%$ for IC 418 and $\sim 10\%$ for NGC 6826. Taking into account the uncertainties in count rates, plasma temperatures, and absorption column densities, the X-ray luminosities of these two sources shown in Table 2 can be higher by 50%. Even then, the locations of these two sources in the L_X/L_{wind} vs. T_{eff} (Fig. 5-b) and L_X/L_{wind} vs. T_X (Fig. 5-c) plots still fall below the theoretical tracks. Contrary to IC 418 and NGC 6826, the data point of NGC 2392 is well above the theoretical tracks in the L_X/L_{wind} vs. T_X plot (Fig. 5-c). We will discuss later in section 4.2 the X-ray peculiarities of NGC 2392.

It has been suggested that the time-scales for the effects of stellar wind shock-heated plasma in PNe is short, $\lesssim 5,000$ yr (Ruiz et al. 2011; Kastner et al. 2012). To investigate the time evolution of the hot bubbles of PNe, we have plot in Figure 6 the X-ray temperature of the PNe in our sample with H-rich stellar winds against the radius of their hot bubbles (top panel) and the effective temperature of their CSPNe (middle panel). The top panel of this figure shows an apparent anti-correlation between the X-ray temperature and hot bubble radius, i.e., as the hot bubble expands, the X-ray temperature of the plasma seems to decrease. The comparison of the data points with the theoretical tracks on this plot reveals that we may be comparing PNe descending from progenitors of different initial masses. This is more clearly illustrated in the middle panel plotting T_X against T_{eff} ; PNe with more massive central stars produce hotter X-ray-emitting plasma because they reach a high wind power in a short time-scale, when the hot bubble is still small in size. The plot of X-ray surface brightness (S_X) against the star effective temperature, in the bottom panel of Figure 6, further supports this conclusion. The value of S_X does not vary much as the star moves along the horizontal track of the post-AGB evolution, but it depends strongly on the mass of the central star. PNe with massive central stars rapidly inject larger amounts of wind mechanical energy into small-sized bubbles, resulting not only in higher plasma temperatures, but also in higher X-ray surface brightnesses.

Finally, it is interesting to note the persistent absence of limb-brightening in the spatial distribution of diffuse X-ray emission from hot bubbles of PNe (see also Kastner et al. 2012). In particular, the diffuse X-ray emission from IC 418, NGC 2392, and NGC 6826 does not show clear evidence for limb-brightening (Fig. 2), suggesting that the X-ray-emitting plasma may fill a significant fraction of the nebular shell. Whereas models of hot bubbles with heat conduction predict a limb-brightened morphology for this diffuse emission, it has been noted that even a small amount of interstellar extinction may reduce significantly the center-to-limb

emission contrast because the soft emission from the cooler plasma close to the nebular rim is more easily absorbed than the harder emission from the hotter plasma inwards (Steffen, Schönberner, & Warmuth 2008). In this respect, the spatial distribution of diffuse X-ray emission from PNe differs notably from that observed in wind-blown bubbles around Wolf-Rayet stars, which show distinct limb-brightened morphologies (e.g., S308, Toalá et al. 2012).

4.2. NGC 2392 – Over-luminous for Its Wind

An inspection of the location of the PNe whose *Chandra* observations are presented in this paper on the different plots shown in Fig. 5 suggests that IC 418 and NGC 6826 are generally a bit under-luminous, whereas NGC 2392 follows the theoretical tracks with the notable exception of its high L_X/L_{wind} in Fig. 5-c. Such peculiar behavior of NGC 2392 is confirmed by comparing its values of L_X/L_{wind} and T_X/T_{shock} to those of the other PNe in Table 3. The diffuse X-ray luminosities of these PNe comprise just minute fractions of their stellar wind mechanical luminosities; however, the diffuse X-ray luminosity of NGC 2392 constitutes a significant fraction, $\sim 10\%$, of its wind mechanical luminosity. In absolute terms, the X-ray luminosity of NGC 2392 exceeds that of many PNe in Table 2, which is puzzling as the stellar wind of the CSPN of NGC 2392 has a relatively low mass-loss rate and a meager terminal velocity of 300 km s^{-1} .

The plasma temperature of NGC 2392 is also puzzling. While the plasma temperatures implied by X-ray spectra of all PNe in Table 2 are lower than the post-shock temperatures of their stellar winds, the observed plasma temperature of NGC 2392 is *higher* than the post-shock temperature expected from its 300 km s^{-1} wind terminal velocity. The influence of heat conduction is expected to lower significantly the plasma temperature from the post-shock temperature (dashed line in Fig. 5-f), which rises with increasing wind velocity, as it is certainly the case for NGC 6826. However, at low wind speeds, early in the evolution of the hot bubble, the influence of heat conduction on plasma temperature is still small, and therefore the plasma temperature is not expected to differ substantially from the post-shock temperature of an adiabatic shock. Yet, the plasma temperature should not exceed the post-shock temperature.

We conclude that the stellar winds of the PNe in our sample are able to power their X-ray-emitting hot gas except for NGC 2392. A wind terminal velocity higher than 300 km s^{-1} is needed for NGC 2392 to raise its expected for L_X and T_X . We note that larger values of the terminal velocity of this wind have been reported by Pauldrach et al. (2004) and Kudritzki et al. (2006), but Herald & Bianchi (2011) have examined these values and found them not compatible with the P-Cygni profiles seen in *FUSE* observations. Considering that an unusual 200 km s^{-1} bipolar outflow has been reported in NGC 2392 (Giesekeing et al. 1985) and that the nebular ionization and expansion velocity are anomalously high, it is possible that the CSPN has a hidden companion and their binary interactions⁸ contribute to the energet-

ics of the nebular interior (Danekhar et al. 2012, Méndez et al., in preparation). Guerrero et al. (2005) suggested that a fraction of the diffuse X-rays from NGC 2392 was associated with this bipolar outflow, an idea later pursued theoretically by Akashi et al. (2008), but the spatial distribution of the diffuse X-ray emission revealed by *Chandra* does not support this hypothesis. Future investigations of the CSPN of NGC 2392 are needed to solve the puzzle of the high X-ray luminosity of its hot interior.

5. SUMMARY AND CONCLUSIONS

We have obtained *Chandra* X-ray observations of three PNe, IC 418, NGC 2392, and NGC 6826, that display narrow nebular O VI absorption lines superposed on the *FUSE* spectra of their CSPNe. Diffuse X-ray emission is detected in each of these three PNe within the sharp innermost optical shell. These detections, together with those in NGC 40, NGC 2371-2, NGC 6543, NGC 7009, and NGC 7662, amount to eight known PNe with hot ($\sim 10^6 \text{ K}$) interior gas in contact with the cool ($\sim 10^4 \text{ K}$) nebular shell whose conduction layers have been confirmed by the presence of collisionally produced O VI. The physical structure of these PNe is thus consistent with that expected from bubble models for H-rich stellar winds including heat conduction (Steffen, Schönberner, & Warmuth 2008) which predict a conduction layer with a steep temperature gradient between the hot interior and the cool nebular shell.

These models also have specific predictions as for the evolution in time of the global X-ray properties of bubble models. To test these predictions, we have compiled relevant information on the X-ray, stellar, and nebular properties of PNe with a bubble morphology. The expectations of bubble models including heat conduction compare positively with the present X-ray observations of PNe with H-rich stellar winds, but those with H-poor [WR] stars present notable discrepancies. There is an apparent anti-correlation between X-ray temperature and hot bubble radius, but we note that this anti-correlation is caused by differences in stellar masses rather than evolutionary stages: PNe with massive central stars are expected to produce hotter X-ray-emitting plasma inside small-sized hot bubbles of higher X-ray surface brightness. On the other hand, PNe with less massive central stars have a slower evolution during the post-AGB phase and inject less amounts of mechanical wind luminosities into larger hot bubbles, resulting in cooler X-ray-emitting plasma.

Finally, we note that the stellar wind of PNe with bubble morphology and hot gas confined in their interiors seems capable of powering their X-ray emission, except for the notable case of NGC 2392. The low speed and small mass-loss rate of its stellar wind result in a low wind mechanical luminosity both in absolute and relative terms compared to other PNe. We suggest that a binary companion may exist and contribute to high energy processes that have provided the additional power to its hot gas.

Support for this work was provided by the National Aeronautics and Space Administration through *FUSE*

imply an orbital separation of 3,400 AU.

⁸ Such interactions exclude the faint companion reported by Ciardullo et al. (1999) to be in a possible binary association because at the distance of $2''65$ from the CSPN of NGC 2392 it would

grant NASA NAG 5-13703 and *Chandra* Award Numbers SAO GO7-8019X and SAO GO1-12029X issued by the *Chandra* X-ray Observatory Center, which is operated by the Smithsonian Astrophysical Observatory for and on behalf of the National Aeronautics Space Administration under contract NASA8-03060. N.R. and M.A.G.

acknowledge partial support by grants AYA 2008-01934 and AYA2011-29754-C03-02 of the Spanish Ministerio de Educación y Ciencia (currently Ministerio de Economía y Competitividad) co-funded by FEDER funds. We thank Dr. Rodolfo Montez for useful discussion on the X-ray luminosity of NGC 40.

Facilities: *Chandra* (ACIS-S), HST (WFPC2), FUSE.

REFERENCES

- Akashi, M., Meiron, Y., & Soker, N. 2008, *New Astr.*, 13, 563
 Arnaud, K. A. 1996, *Astronomical Data Analysis Software and Systems V*, 101, 17
 Barker, T. 1991, *ApJ*, 371, 217
 Bombeck, G., Köppen, J., & Bastian, U. 1986, *New Insights in Astrophysics. Eight Years of UV Astronomy with IUE*, 263, 287
 Cerruti-Sola, M., & Perinotto, M. 1985, *ApJ*, 291, 237
 Cerruti-Sola, M., & Perinotto, M. 1989, *ApJ*, 345, 339
 Chu, Y.-H., Gruendl, R. A., & Guerrero, M. A. 2004, in Meixner M., Kastner J.H., Balick B., Soker N., eds, *Proc. Asymmetrical Planetary Nebulae III: Winds, Structure and the Thunderbird*. ASP Conference Proceedings, Vol. 313. San Francisco: Astronomical Society of the Pacific, p. 254
 Chu, Y.-H., Guerrero, M. A., Gruendl, R. A., Williams, R. M., & Kaler, J. B. 2001, *ApJ*, 553, L69
 Ciardullo, R., Bond, H. E., Sipior, M. S., et al. 1999, *AJ*, 118, 488
 Clark, D.M., López, J.A., Steffen, W., & Richer, M.G. 2012, *AJ*, in press (arXiv:1210.2445)
 Danehkar, A., Frew, D. J., Parker, Q. A., & De Marco, O. 2012, in Richards M.T., Hubeny I., eds, *Proc. IAU Symp. 282, From Interacting Binaries to Exoplanets: Essential Modeling Tools*, Cambridge Univ. Press, Cambridge, p. 470
 Dixon, W. V., Sahnou, D. J., Barrett, P. E., et al. 2007, *PASP*, 119, 527
 Ferland, G. J., Korista, K. T., Verner, D. A., et al. 1998, *PASP*, 110, 761
 Frew, D. J. 2008, Ph.D. Thesis, Department of Physics, Macquarie University, Sydney, Australia
 Gieseking, F., Becker, I., & Solf, J. 1985, *ApJ*, 295, L17
 Gruendl, R. A., Guerrero, M. A., Chu, Y.-H., & Williams, R. M. 2006, *ApJ*, 653, 339
 Gruendl, R. A., Chu, Y.-H., & Guerrero, M. A. 2004, *ApJ*, 617, L127
 Guerrero, M. A., Chu, Y.-H., Gruendl, R. A., & Meixner, M. 2005, *A&A*, 430, L69
 Guerrero, M. A., Chu, Y.-H., & Miranda, L.F. 2004, *AJ*, 128, 1694
 Guerrero, M. A., & De Marco, O. 2013, submitted to *A&A*
 Guerrero, M. A., Ramos-Larios, G., & Massa, D. 2010, *PASA*, 27, 210
 Henry, R.B.C., Kwitter, K.B., & Bates, J.A. 2000, *ApJ*, 531, 928
 Herald, J. E., & Bianchi, L. 2011, *MNRAS*, 417, 2440
 Iping, R. C., Sonneborn, G., & Chu, Y.-H. 2002, *Bulletin of the American Astronomical Society*, 34, 1254
 Kastner, J. H., Montez, R., Jr., Balick, B., & De Marco, O. 2008, *ApJ*, 672, 957
 Kastner, J. H., et al. 2012, *AJ*, 144, 58
 Kastner, J. H., Soker, N., Vrtilik, S. D., & Dgani, R. 2000, *ApJ*, 545, L57
 Kastner, J. H., Vrtilik, S. D., & Soker, N. 2001, *ApJ*, 550, L189
 Kudritzki, R.P., Urbaneja M.A., & Puls J. 2006, in Barlow M.J., Méndez R.H., eds, *Proc. IAU Symp. 234, Planetary Nebulae in our Galaxy and Beyond*. Cambridge Univ. Press, Cambridge, p. 119
 Kwok, S. 1983, in Flower D.R., eds, *Proc. IAU Symp. 103, Planetary Nebulae*. Cambridge Univ. Press, Cambridge, p. 293
 Latter, W. B., Dayal, A., Biegging, J. H., et al. 2000, *ApJ*, 539, 783
 Marcolino, W. L. F., Hillier, D. J., de Araujo, F. X., & Pereira, C. B. 2007, *ApJ*, 654, 1068
 Marten, H., & Schönberner, D. 1991, *A&A*, 248, 590
 Mellema, G. 1994, *A&A*, 290, 915
 Mellema, G. 2004, *A&A*, 416, 623
 Méndez, R. H., Kudritzki, R. P., Herrero, A., Husfeld, D., & Groth, H. G. 1988, *A&A*, 190, 113
 Montez, R., Jr., Kastner, J. H., De Marco, O., & Soker, N. 2005, *ApJ*, 635, 381
 Moos, H. W., Cash, W. C., Cowie, L. L., et al. 2000, *ApJ*, 538, L1
 Pauldrach, A. W. A., Hoffmann, T. L., & Méndez, R. H. 2004, *A&A*, 419, 1111
 Perinotto, M., Schönberner, D., Steffen, M., & Calonaci, C. 2004, *A&A*, 414, 993
 Pottasch, S. R., Bernard-Salas, J., & Roellig, T. L. 2008, *A&A*, 481, 393
 Pottasch, S. R., Bernard-Salas, J., Beintema, D. A., & Feibelman, W. A. 2004, *A&A*, 423, 593
 Ruiz, N., Guerrero, M.A., Chu, Y.-H., & Gruendl, R.A. 2011, *AJ*, 142, 91
 Sahnou, D. J., Moos, H. W., Ake, T. B., et al. 2000, *ApJ*, 538, L7
 Schmidt-Voigt, M., & Köppen, J. 1987, *A&A*, 174, 223
 Schönberner, D., Steffen, M., & Warmuth, A. 2006, in Barlow M.J., Méndez R.H., eds, *Proc. IAU Symp. 234, Planetary Nebulae in our Galaxy and Beyond*. Cambridge Univ. Press, Cambridge, p. 161
 Shull, J. M., & van Steenberg, M. 1982, *ApJS*, 48, 95
 Spitzer, L. 1962, *Physics of Fully Ionized Gases*, New York: Interscience (2nd edition), 1962
 Steffen, M., Sandin, C., Jacob, R., & Schönberner, D. 2012, in Manchado A., Stanghellini L., and Schönberner D., eds, *Proc. IAU Symp. 283: Planetary Nebulae: An Eye to the Future*. Cambridge Univ. Press, Cambridge, p. 215
 Steffen, M., Schönberner, D., & Warmuth, A. 2008, *A&A*, 489, 173
 Surendiranath, R., & Pottasch, S. R. 2008, *A&A*, 483, 519
 Tinkler, C. M., & Lamers, H. J. G. L. M. 2002, *A&A*, 384, 987
 Toalá, J. A., Guerrero, M. A., Chu, Y.-H., et al. 2012, *ApJ*, 755, 77
 Villaver, E., Manchado, A., & García-Segura, G. 2002, *ApJ*, 581, 1204
 Volk, K., & Kwok, S. 1985, *A&A*, 153, 79
 Weaver, R., McCray, R., Castor, J., Shapiro, P., & Moore, R. 1977, *ApJ*, 218, 377
 Zhekov, S. A., & Perinotto, M. 1998, *A&A*, 334, 239